NANO LETTERS
Letter
Cite This: Nano Lett. 2019, 19, 7006−7012
pubs.acs.org/NanoLett

STM Imaging of Electron Migration in Real Space and Time: A Simulation Study

YanHo Kwok,[†,‡] GuanHua Chen,[†] and Shaul Mukamel[§]

[†]Department of Chemistry, The University of Hong Kong, Pofkulam Road, Hong Kong
[‡]QuantumFabless Limited, Sha Tin, Hong Kong
[§]Department of Chemistry and Physics and Astronomy, University of California, Irvine, California 92617, United States

Supporting Information

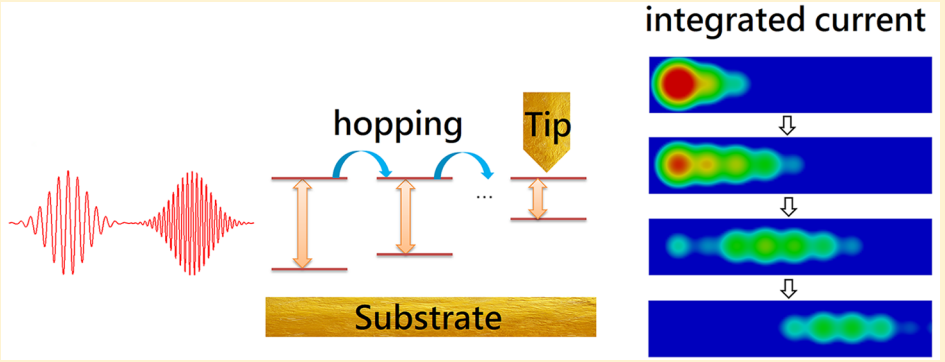

ABSTRACT: Using a simulation protocol that mimics ultrafast scanning tunneling microscopy (STM) experiments, we demonstrate how pump−probe ultrafast STM may be used to image electron migration in molecules. Two pulses are applied to a model system, and the time-integrated current through the tip is calculated versus the delay time and tip position to generate STM images. With suitable pump and probe parameters, the images can track charge migration with atomistic spatial and femtosecond temporal resolutions.

KEYWORDS: *Scanning tunneling microscopy, optical pump−probe, charge migration, time-dependent simulation*

Imaging electron hopping among atoms in real time has been a long-time dream. The advancement of ultrafast pulses has made it possible to directly probe electron dynamics,[1−4] which typically occur on attosecond to femtosecond (10^{-18} to 10^{-15}) time scales, by time-resolved pump−probe spectroscopy. Electronic motion in molecules,[5,6] electron transfer,[7] and light-induced electron tunneling[8] have been reported. However, these experiments lack direct spatial resolution.

In a separate development, scanning tunneling microscopy (STM) techniques have been widely used for visualizing samples with precise atomistic spatial resolution. A combination of STM and optical pump−probe techniques can provide both atomic spatial and ultrafast temporal resolutions.[9−16] Recently, the ultrafast terahertz STM (THz-STM) technique has been used to visualize the picosecond vibrational motion of a single pentacene molecule.[17] In the experiment, pump and probe single-cycle laser pulses are focused onto the STM junction to create ultrafast transient modulation of the bias voltage. This induces a transient tunneling current through the molecular orbital of the molecule, which is recorded by the tip to produce an image of the orbital. By varying the time delay between pump and probe pulses, imaging the molecular orbital variation with the molecular vibration becomes feasible, leading to a direct probe of molecular vibrations. These experiments represent an exciting step toward imaging single molecules and their nuclear dynamics in real time.[17−20] Imaging electronic dynamics has not been reported yet.

In this paper, we demonstrate how the ultrafast pump−probe STM technique can be used to image electron migration processes in molecules. Using a state-of-the-art time-dependent simulation protocol for open quantum systems, we carry out a real time simulation of a model system subjected to ultrafast pump−probe pulses underneath an STM tip. The integrated current measured at the STM tip for different pump−probe delays provides femtosecond snapshots of the dynamics, whereas its location at different atomic sites gives a fine spatial resolution, generating direct and intuitive images of the charge migration process.

We model the STM junction as an open electronic system which consists of a central region coupled to two semi-infinite electrodes (tip and substrate), as shown in Figure 1. The central region is a 10-site tight binding model system where each site has a single HOMO and LUMO orbital. The

Received: June 13, 2019
Revised: September 11, 2019
Published: September 11, 2019

DOI: 10.1021/acs.nanolett.9b02389
Nano Lett. 2019, 19, 7006−7012

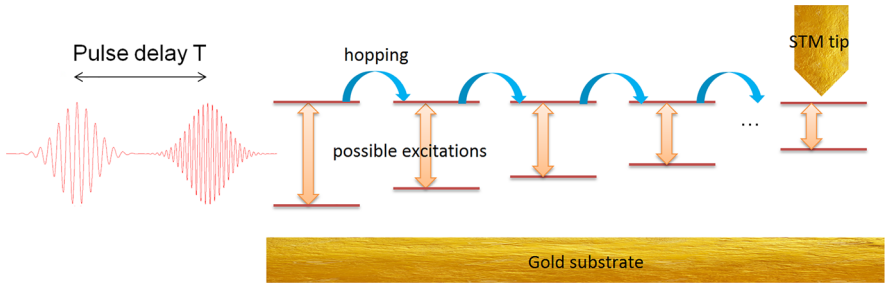

Figure 1. Model system used in this study. The system has 10 sites with varying HOMO−LUMO gaps (marked by the red horizontal lines). Blue arrows indicate hopping among sites. Orange arrows indicate possible optical excitations (with nonzero transition dipole).

Liouville−von Neumann equation for the reduced single-electron density matrix of the central region is propagated numerically.[21,22] Making the dipole approximation for the matter/light interaction, the time-dependent Hamiltonian of the system is written as $\mathbf{h}(t) = \mathbf{h}(0) + \boldsymbol{\mu}\cdot E(t)$, where $\mathbf{h}(0)$ is the initial Hamiltonian without the electric field and $\boldsymbol{\mu}$ is the dipole operator. $E(t) = \mathcal{E}_1(t)\cos(\omega_1 t) + \mathcal{E}_2(t)\cos(\omega_2 t)$ is the pump and probe electric field, where $\mathcal{E}_1(t)$ and ω_1 denote the Gaussian envelope and frequency of the pump pulse, and $\mathcal{E}_2(t)$ and ω_2 denote the corresponding quantities of the probe. The laser pulses affect the system in two ways. First, they can resonantly excite electrons from HOMO to LUMO. Second, when the polarization of the electric field has a component in the tip−substrate direction, a transient bias voltage can be induced due to field enhancement, which can cause an injection of electrons from the electrodes. In the THz-STM experiments,[9,16,17] asymmetric single-cycle pulses have been used to induce an asymmetric transient voltage that drives the tunneling of electrons in or out of the system. In our simulations, the pump selectively excites a particular site, creating a localized charge, and the probe tracks the electron populations of the sites. We use multicycle Gaussian pulses whereby the electric field is perpendicular to the tip−substrate axis. This is designed to excite the molecule, which lies flat approximately on the substrate, and eliminate the induced transient bias across the junction and the tunneling current due to the field emission. The current through the STM is caused mainly by the electron population change at the site. This configuration is similar to that in shaken pulse-pair-excited STM.[23,24] We also consider the case where the electric field is parallel to the tip−substrate axis and estimate the electron injection by taking into account the induced transient voltage. Simulation results presented in the Supporting Information reveal that the technique can still track the charge migration in that case. The pump−probe STM signal depends on the fourth-order current response that scales as $O(\mathcal{E}_1^2\mathcal{E}_2^2)$, in which the pump pulse first interacts with the molecule twice to create a population followed by probe pulse that detects it. Unlike typical pump−probe experiments which measure the change in the reflectivity, we directly measure the current. Figure 2 shows the two ladder diagrams for the signal in a two-level model system. The left diagram describes the stimulated emission, in which the probe stimulates the excited populations back to ground state with the emission of a photon. The right diagram describes the reduction of absorption and current signal due to the smaller ground-state populations, known as ground-state bleaching. These two processes contribute to the current signal with the same sign, and the diagrams are similar to those in

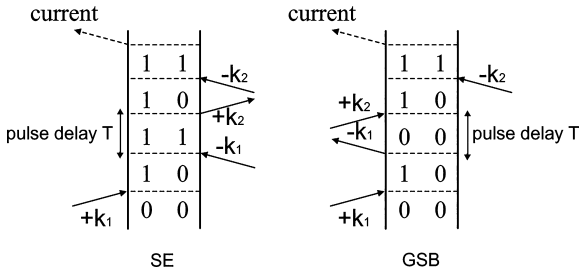

Figure 2. Ladder diagrams for the simulated emission (SE) and ground-state bleaching (GSB) processes in pump−probe STM. The left diagram describes stimulated emission, in which the probe stimulates the excited populations back to the ground state with the emission of a photon. The right diagram describes the reduction of absorption and current signal due to the lower ground-state populations, known as ground-state bleaching.

two-dimensional photocurrent spectroscopy[25,26] but with $T_1 = T_3 = 0$.

To obtain the current response in the desired order and phase-matching condition, we follow the phase-matching approach.[27,28] Details are presented in the Methods section.

STM electronics is too slow to resolve the fast current dynamics, and the time-integrated current $\int_{-\infty}^{\infty} J(t)\mathrm{d}t$, also known as rectified component, is measured. Nevertheless, ultrafast time resolution is achieved by varying the delays between femtosecond pulses. In the following, we show how the integrated current can be used to track the time-resolved charge migration.

In the 10-site tight binding model system, each site has a single HOMO and LUMO orbital below and above the Fermi level of entire system, respectively. The substrate is assumed to couple with all orbitals, whereas the tip couples only to the LUMO of a single site, selected by the tip position, as sketched in Figure 1. The energy of the LUMO of all sites are 1.5 eV above the Fermi level, whereas the HOMO values of the 10 sites are 4.1, 3.7, 3.3, 2.9, 2.5, 2.1, 1.7, 1.3, 0.9, and 0.5 eV below the Fermi level. The LUMO energies are assumed to be the same for simplicity. In the Supporting Information, we also consider a system with varying LUMO energies. The Fermi level of the system is related to the work function of the electrodes and is taken to be −5.1 eV, mimicking gold. The work function does not affect the signals because we do not apply the electric field along the tip−substrate direction, and thus tunneling field emission is excluded. The hopping elements among the LUMO are taken to be 0.05 eV to allow charge migration. Transition dipole moments between the HOMO and LUMO of each site are 1 *e*Å. The tunneling current is sensitive to the distance between the molecule and

DOI: 10.1021/acs.nanolett.9b02389
Nano Lett. 2019, 19, 7006−7012

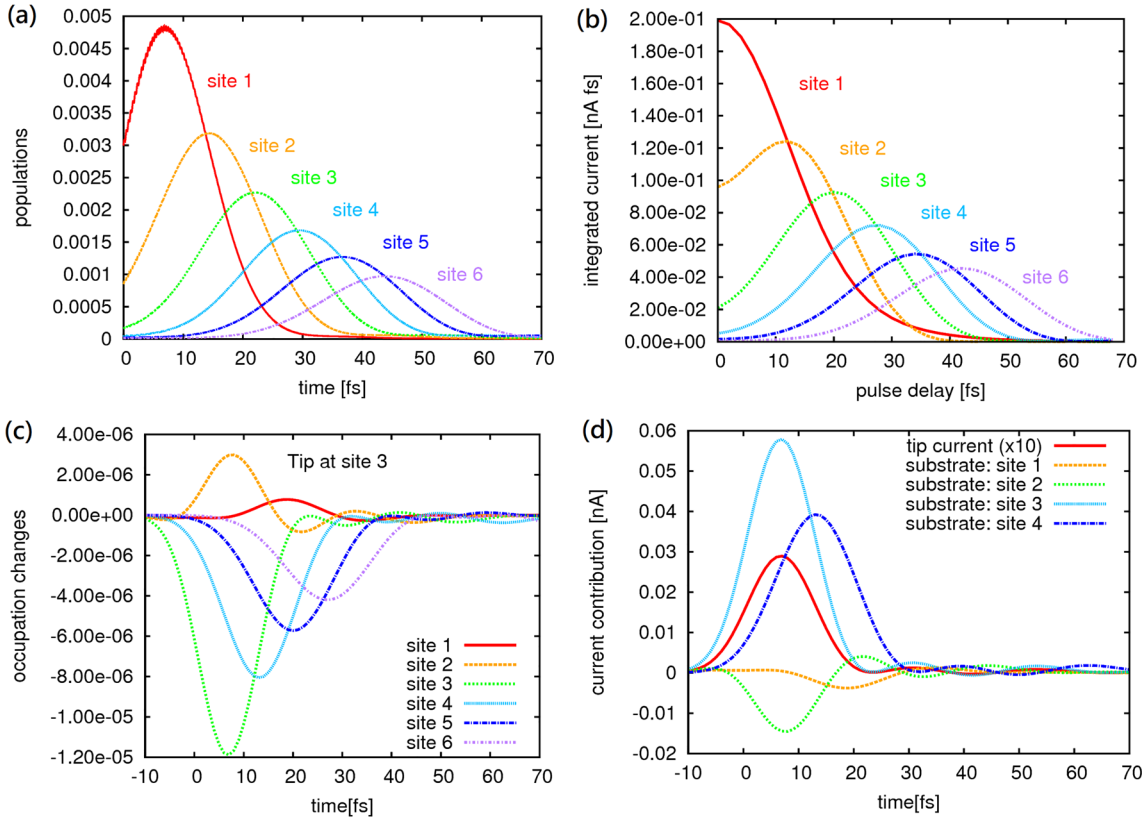

Figure 3. (a) LUMO populations of sites 1−6 after the arrival of the pump. (b) Integrated current versus pump−probe delay when the tip is located at sites 1−6. For the tip located at site 1, the magnitude is reduced by a factor of 3. In (c) and (d), the tip is placed at site 3, with a pulse delay of 20 fs. (c) Fourth-order occupation changes of LUMO of sites 1−6 after arrival of the probe pulse. (d) Fourth-order tip current (red curve, magnified by 10 times) and substrate current contribution from the LUMO of sites 1−4 after arrival of the probe.

electrodes, typically 3−10 Å. We assume a tip−substrate distance of 1 nm, and the coupling between the molecule and the electrodes enters through the line width matrix. The line width matrix of the substrate is diagonal with a value equal to 0.08 eV for the HOMO of sites and 0.02 eV for the LUMO of sites. The substrate thus couples to all sites identically, but holes will leave the system faster than electrons, resulting in a charged site after excitation. The line width matrix of the tip is equal to 0.001 eV for the LUMO of the site selected by the tip and zero otherwise. The line width matrices determine the dissipation rate of the excited-state populations. In our model, the line width due to the substrate is comparable to the hopping among sites, thus these events occurs in a similar tens of femtoseconds time scale. In practice, the molecule may be placed on a thin decoupling layer to avoid strong coupling with the substrate. In the Supporting Information, we present the simulation results for that configuration, where coupling to the substrate is reduced, and show that this technique can still track the charge migration.

We tune the central frequency of the pump to be resonant with the 5.6 eV HOMO−LUMO gap of site 1, with a maximum strength of 0.01 V/Å and full width at half-maximum (fwhm) equal to 20 fs, such that the pump pulse only excites the first site. The central frequency of the probe, ω_2, is chosen to be resonant with the HOMO−LUMO gap of the site under the STM tip, and the width of the probe is the same as that of the pump. The electric field is assumed to be perpendicular to the tip direction. Therefore, electron injection or field emission due to induced transient voltage across the junction is not possible. By placing the STM tip at different positions and varying the probe pulse, we are able to track the charge migration via the integrated current by varying the pump−probe delay. For instance, to track the population on site 3, we position the STM tip at that site so that it couples to its LUMO. We further tune the central frequency of the probe ω_2 to be resonant with the HOMO−LUMO gap of site 3 so that the probe will mainly detect the population of that site. This reduces noise due to current created by the excitation of nearby sites. All simulations assume 300 K temperature and 0 DC bias voltage. A DC bias voltage would produce a static electric field across the junction that affects the tendency of electrons to tunnel to the tip or substrate as well as the magnitude of the current. Nevertheless, as long as the integrated current is proportional to the time-dependent populations, it can be used to track the charge migration.

The simulation results are summarized in Figure 3. Figure 3a shows the time-dependent populations of the LUMO of sites 1−6 induced by the pump located at site 1 and centered at time zero. The total population is fractional because it is the expectation value. The population at site 1 increases first. Excited populations then gradually migrate to other sites. At the same time, some electrons on the LUMO leak into the substrate, thus causing population decay. Figure 3a is produced by the simulation in which the tip is located at site 2, but the results are similar for the tip at the other sites. Afterward, the probe pulse arrives after a pulse delay T, and the integrated current induced is measured. Figure 3b shows the integrated current versus the pulse delay when the tip is located at different sites (ω_2 is also adjusted accordingly). Except for site 1, the signal generally resembles the population curves. On a

DOI: 10.1021/acs.nanolett.9b02389
Nano Lett. 2019, 19, 7006−7012

closer look, we see that the integrated current peaks occur slightly earlier than the corresponding populations. This is due to the current from nearby sites which can also be excited by the probe pulse, and the electrons can then migrate to the site under the tip, resulting in a current. To reduce this undesired effect, we can use a narrower bandwidth probe at the expense of the temporal resolution. Further discussion of the effect of pulse width and frequency can be found in the Supporting Information, where we compare results with different pulse widths and quantify the current contributed by unwanted excitations of nearby sites. In Figure 3c,d, the tip is located at site 3 and pulse delay is 20 fs. These will be discussed later.

The current generation process for this model is represented by the ladder diagrams shown in Figure 4. Here, $|0\rangle$ and $|1\rangle$ denote the HOMO and LUMO of the first site, respectively. The pump excites electrons from HOMO to LUMO at this site, creating a population on its LUMO. Depending on the pulse delay, the electrons may then migrate to the LUMO of the next site $|1'\rangle$ or remain on the LUMO of the original site, as shown in Figure 4a,b, respectively. This electron migration leads to the time-dependent populations shown in Figure 3a. After the pulse delay T, we probe the time-dependent populations with the probe pulse and measure the induced time-integrated current signal. The induced current may pass through either the tip or the substrate depending on the tip position. Significant current will pass through the tip when the electron resides on the LUMO of the STM tip-probing site. Otherwise, electrons will leak through the substrate, which results in a zero net current (because holes also move this way). The time-integrated current signal is therefore proportional to the population of the tip-probing site at the probe arrival time. It is also possible that, after repopulation by the probe, the electron could migrate to the tip-probing site from nearby sites and exit through the tip. This also results in net-induced current, making the induced current deviate from the LUMO population of the tip-probing site. This process can be minimized by tuning the probe frequency to be resonant with the HOMO−LUMO gap of the tip-probing site so that repopulation of nearby sites is suppressed. Figure 3c shows the fourth-order occupation change (diagonal elements of fourth-order reduced single-electron density matrix) of the LUMO of sites 1−6 after the probe when the tip is located at site 3 and pulse delay is equal to 20 fs. The induced change of population at site 3 is largest due to matching frequency with the HOMO−LUMO gap; however, the repopulation of nearby sites is also significant. The induced population on site 3 will then move to the tip or the substrate, creating a transient current which lasts for tens of femtoseconds, as shown in Figure 3d (red and cyan curves). The transient current passing through the tip creates a net-integrated current that reflects the site 3 population. The induced populations on the other sites will either leave to the substrate (also shown in Figure 3d) or migrate to site 3 and leave to the tip.

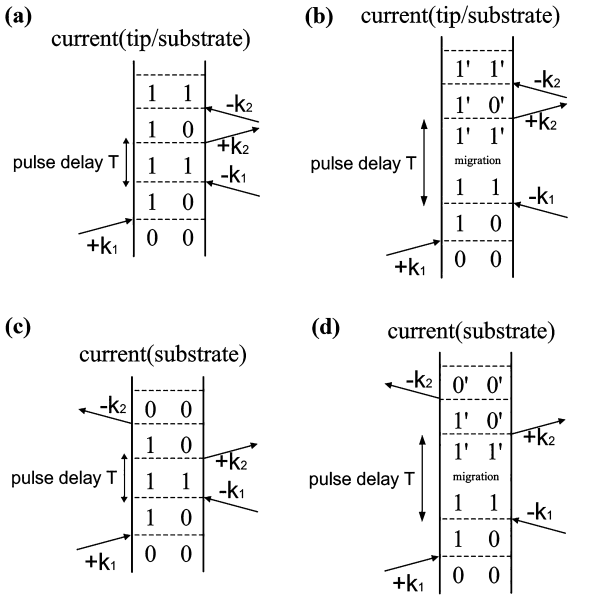

Figure 4. Ladder diagrams for the pump−probe STM current generation. $|0\rangle$ and $|1\rangle$ denote HOMO and LUMO of the first site. $|0'\rangle$ and $|1'\rangle$ denote HOMO and LUMO of the site to which the electron migrated. The pump excites electrons from HOMO to LUMO of the first site, creating a population on its LUMO. Depending on the pulse delay, the electrons may then migrate to the LUMO of the next site $|1'\rangle$ or remain on the LUMO of the original site. After the pulse delay T, we probe the time-dependent populations with the probe pulse and measure the induced time-integrated current signal. Diagrams (a) and (b) correspond to the generation of electron current from the LUMO of the first site and the other site, respectively, whereas diagrams (c) and (d) correspond to the generation of a hole current from the HOMOs.

Assuming a spherical localized orbital for the LUMO at each site and projecting the integrated current signal in real space, we can calculate the corresponding ultrafast STM images. The resulting series of images versus pulse delay produce an animation of the charge migration across the system. The left panel of Figure 5 depicts the snapshots of animation generated in this way with pulse delays of 0, 16, 32, and 48 fs. For comparison, we also project the LUMO's occupation of the sites onto real space to obtain the time-dependent electron density images, and the results are shown in the right panel of Figure 5. It is evident that the pump−probe ultrafast STM can track charge migration in this model system.

The development of ultrafast pump−probe STM has made it possible to image single-molecule dynamics with atomic resolution because the temporal resolution is no longer limited by electronics but rather determined by applied laser pulses. We have shown how it can be used to produce a movie of electron migration in our model system. Our model assumes a molecular structure with units of varying HOMO−LUMO gaps, which is required for selectively exciting and probing the populations at different sites. The gradually decreasing HOMO−LUMO gaps used here are not required for our technique to work. In reality, we can construct an oligomer from molecular units of different length or substituted with different functional groups, so that each unit has a different HOMO−LUMO gap. One example is an oligomer constructed with phenylacetylene units. Different lengths of para-linked phenylacetylene oligomer segments were shown to have different HOMO−LUMO gaps from around 3 to 4 eV.[29] We can connect such segments at the meta-position to create a conjugated system in which each segment has a different HOMO−LUMO gap and the electron can migrate among them. Given the wide range of potential applications of pump−probe spectroscopy, it can be envisioned that ultrafast pump−probe STM will also find applications in tracking various electronic dynamic processes. Technical challenges to be solved include how to apply it to complex systems and how to make the excitations as local as possible.

DOI: 10.1021/acs.nanolett.9b02389
Nano Lett. 2019, 19, 7006−7012

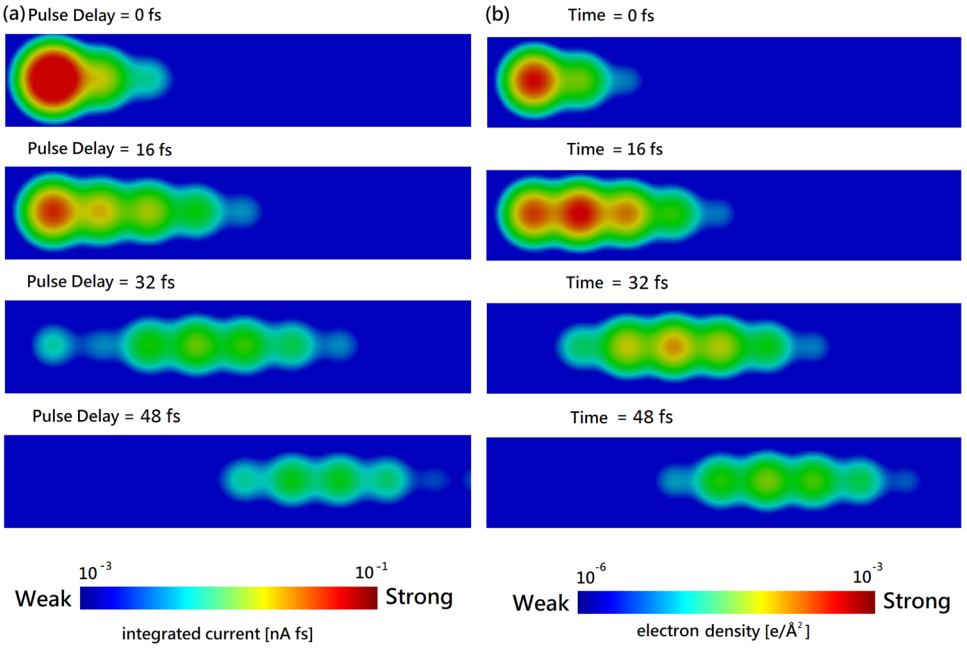

Figure 5. Left panel: computed pump–probe STM images with various pulse delays as indicated. Color reflects the magnitude of integrated current on a log scale (projected on real space). Right panel: electron density images (obtained by projecting occupation of LUMOs on real space) at the same times. Color reflects the magnitude of electron density on a log scale.

Methods. We modeled the STM junction as an open electronic system which consists of a central region of interest D coupled to two semi-infinite electrodes (tip and substrate), as shown in Figure 1. Assuming that the tip and substrate do not couple directly to each other, the Liouville–von Neumann equation for the reduced single-electron density matrix (RSDM) of the central region $\boldsymbol{\sigma}_D$ is given by[21,22]

$$i\frac{d}{dt}\boldsymbol{\sigma}_D(t) = [\mathbf{h}_D, \boldsymbol{\sigma}_D] - \sum_\alpha [\boldsymbol{\varphi}_\alpha(t) - \boldsymbol{\varphi}_\alpha^\dagger(t)] \tag{1}$$

where $\mathbf{h}_D(t)$ is the Hamiltonian for the central region and

$$\boldsymbol{\varphi}_\alpha(t) = i\int_{-\infty}^{t} d\tau[\mathbf{G}_D^<(t,\tau)\boldsymbol{\Sigma}_\alpha^>(\tau,t) - \mathbf{G}_D^>(t,\tau)\boldsymbol{\Sigma}_\alpha^<(\tau,t)] \tag{2}$$

is the dissipative matrix between the system and α, which denotes *tip* or *substrate*. $\mathbf{G}_D^{>,<}$ and $\boldsymbol{\Sigma}_D^{>,<}$ denote the greater and lesser Green's function of device and self-energy due to electrode α, respectively. The dissipative term represents the interactions, including the exchange of electrons and energy, between the device and electrodes. Its trace results in the time-dependent electric current passing from electrode α into the device region.

$$J_\alpha(t) = i\mathrm{Tr}[\boldsymbol{\varphi}_\alpha(t) - \boldsymbol{\varphi}_\alpha^\dagger(t)] \tag{3}$$

We have employed the wide band limit approximation,[30] which assumes that the electrodes have infinitely large band widths and energy-independent broadening matrix. The dissipative matrix can then be decomposed into a sum of auxiliary matrices by expanding the Fermi–Dirac distribution with Padé spectrum decomposition:[31,32]

$$f(\varepsilon) \approx \frac{1}{2} - \sum_p \left(\frac{R_p}{\varepsilon + iz_p} + \frac{R_p}{\varepsilon - iz_p}\right) \tag{4}$$

$$\boldsymbol{\varphi}_\alpha(t) = \frac{i}{4}[2\boldsymbol{\sigma}_D(t) - \mathbf{I}]\boldsymbol{\Gamma}_\alpha + \sum_p \boldsymbol{\varphi}_{\alpha,p}(t) \tag{5}$$

where $\boldsymbol{\Gamma}_\alpha$ is the line width matrix due to coupling to electrode α and $\mathbf{I}$ is the identity matrix. $\boldsymbol{\varphi}_{\alpha,p}(t)$ are decomposed dissipative matrices that sum up to the dissipative term, defined by

$$\boldsymbol{\varphi}_{\alpha,p}(t) = -iR_p\int_{-\infty}^{t} d\tau \mathbf{G}_D^r(t,\tau)\boldsymbol{\Gamma}_\alpha \exp\left(-i\int_t^\tau dt' \varepsilon_{\alpha,p}(t')\right) \tag{6}$$

These dissipative matrices satisfy the equations of motion (EOM)

$$i\frac{d}{dt}\boldsymbol{\varphi}_{\alpha,p}(t) = -iR_p\boldsymbol{\Gamma}_\alpha + \left[h_D - \frac{i}{2}\boldsymbol{\Gamma} - \varepsilon_{\alpha,p}(t)\right]\boldsymbol{\varphi}_{\alpha,p}(t) \tag{7}$$

where $\varepsilon_{\alpha,p}(t) = \mu_\alpha + iz_p + \Delta_\alpha(t)$ and $\boldsymbol{\Gamma} = \boldsymbol{\Gamma}_{tip} + \boldsymbol{\Gamma}_{substrate}$. μ_α and $\Delta_\alpha(t)$ are the equilibrium chemical potential and time-dependent bias voltage of lead α. Equations 1, 5, and 7 form a closed set. The time-dependent RSDM can be obtained by propagating these EOM with proper initial conditions. We assume that the system is initially at equilibrium. The initial values of RSDM and auxiliary matrices can therefore be obtained by standard non-equilibrium Green's function calculations.

The interaction between the electronic system and the laser pulses is described by the dipole approximation, thus the time-dependent device Hamiltonian is written as

$$\mathbf{h}_D(t) = \mathbf{h}_D(0) + \boldsymbol{\mu}\cdot E(t)$$

where $\mathbf{h}_D(0)$ is the initial device Hamiltonian where an electric field is absent, $\boldsymbol{\mu}$ is the dipole matrix, $E(t)$ is the time-dependent electric field due to the pump and probe, given by

$$E(t) = \mathcal{E}_1(t)\cos(\omega_1 t) + \mathcal{E}_2(t)\cos(\omega_2 t)$$

DOI: 10.1021/acs.nanolett.9b02389
Nano Lett. 2019, 19, 7006–7012

in which $\mathcal{E}_1(t)$ and ω_1 denote the Gaussian envelope and frequency of the pump pulse and $\mathcal{E}_2(t)$ and ω_2 denote the corresponding quantities of the probe. Propagating the EOM described above results in the total time-dependent response to all orders. In simulating pump−probe STM, we retain the fourth-order current response that scales as $O(\mathcal{E}_1^2\mathcal{E}_2^2)$.

To extract the current response in the desired order and phase-matching condition, we follow the phase-matching approach,[27,28] originally applied to simulate two-dimensional optical spectra with time-domain propagation. Removal of lower-order responses is possible by running several simulations with each of the pulses being switched on or off. The fourth-order current response is calculated by

$$J^{(4)}(t) = \sum_{p,q,r,s=0}^{1} (-1)^{p+q+r+s} J_{p,q,r,s}(t) \tag{8}$$

where $J_{p,q,r,s}(t)$ is the time-dependent current obtained from a simulation with the following incident field:

$$E(t) = \frac{p}{2}\mathcal{E}_1(t)\exp(-i\omega_1 t) + \frac{q}{2}\mathcal{E}_1(t)\exp(+i\omega_1 t) + \frac{r}{2}\mathcal{E}_2(t)\exp(-i\omega_2 t) + \frac{s}{2}\mathcal{E}_2(t)\exp(+i\omega_2 t) \tag{9}$$

in which p, q, r, and s are either 1 or 0, indicating the pulse is present or not in that particular simulation. One can show that by the summation given in eq 8, the lowest-order response with respect to the incident field will be $O(\mathcal{E}_1^2\mathcal{E}_2^2)$ with the desired phase-matching condition of $k = k_1 - k_1 + k_2 - k_2$. Any responses that are of lower order or same total order, such as $O(\mathcal{E}_1^3\mathcal{E}_2)$, will be canceled out by the summation.

Besides the phase-matching approach, we can alternatively expand the EOM in previous section, eqs 1 and 7, perturbatively. We verified that two approaches agree as long as the amplitudes of pulses are not strong. Our simulations were carried out using the phase-matching approach.

■ ASSOCIATED CONTENT

Supporting Information

The Supporting Information is available free of charge on the ACS Publications website at DOI: 10.1021/acs.nanolett.9b02389.

Additional experimental details and supporting figures (PDF)

■ AUTHOR INFORMATION

ORCID

YanHo Kwok: 0000-0003-1325-4416
GuanHua Chen: 0000-0001-5015-0902
Shaul Mukamel: 0000-0002-6015-3135

Notes

The authors declare no competing financial interest.

■ ACKNOWLEDGMENTS

The support from the Hong Kong Research Grant Council (HKUST9/CRF/11G, HKU700912P, HKU7007-11P), the University Grant Council (AOE/P-04/08), is gratefully acknowledged. S.M. acknowledges the support of the National Science Foundation Grant CHE-1663822.

■ REFERENCES

(1) Hu, S. X.; Collins, L. A. *Phys. Rev. Lett.* **2006**, *96*, 073004.
(2) Feng, X.; Gilbertson, S.; Mashiko, H.; Wang, H.; Khan, S. D.; Chini, M.; Wu, Y.; Zhao, K.; Chang, Z. *Phys. Rev. Lett.* **2009**, *103*, 183901.
(3) Vrakking, M. J. *Phys. Chem. Chem. Phys.* **2014**, *16*, 2775−2789.
(4) Nisoli, M.; Decleva, P.; Calegari, F.; Palacios, A.; Martin, F. *Chem. Rev.* **2017**, *117*, 10760−10825.
(5) Kraus, P. M.; Mignolet, B.; Baykusheva, D.; Rupenyan, A.; Horný, L.; Penka, E. F.; Grassi, G.; Tolstikhin, O. I.; Schneider, J.; Jensen, F.; et al. *Science* **2015**, *350*, 790−795.
(6) Calegari, F.; Ayuso, D.; Trabattoni, A.; Belshaw, L.; De Camillis, S.; Anumula, S.; Frassetto, F.; Poletto, L.; Palacios, A.; Decleva, P.; et al. *Science* **2014**, *346*, 336−339.
(7) Fohlisch, A.; Feulner, P.; Hennies, F.; Fink, A.; Menzel, D.; Sanchez-Portal, D.; Echenique, P. M.; Wurth, W. *Nature* **2005**, *436*, 373−376.
(8) Uiberacker, M.; Uphues, T.; Schultze, M.; Verhoef, A. J.; Yakovlev, V.; Kling, M. F.; Rauschenberger, J.; Kabachnik, N. M.; Schröder, H.; Lezius, M.; et al. *Nature* **2007**, *446*, 627−632.
(9) Cocker, T. L.; Jelic, V.; Gupta, M.; Molesky, S. J.; Burgess, J. A. J.; Reyes, G. D. L.; Titova, L. V.; Tsui, Y. Y.; Freeman, M. R.; Hegmann, F. A. *Nat. Photonics* **2013**, *7*, 620−625.
(10) Shigekawa, H. Time-Resolved Scanning Tunneling Microscopy. *Compendium of Surface and Interface Analysis*; Springer: Singapore, 2018; pp 749−753.
(11) Jelic, V.; Iwaszczuk, K.; Nguyen, P. H.; Rathje, C.; Hornig, G. J.; Sharum, H. M.; Hoffman, J. R.; Freeman, M. R.; Hegmann, F. A. *Nat. Phys.* **2017**, *13*, 591−598.
(12) Yoshida, S.; Aizawa, Y.; Wang, Z.; Oshima, R.; Mera, Y.; Matsuyama, E.; Oigawa, H.; Takeuchi, O.; Shigekawa, H. *Nat. Nanotechnol.* **2014**, *9*, 588−593.
(13) Wu, S. W.; Ho, W. *Phys. Rev. B: Condens. Matter Mater. Phys.* **2010**, *82*, 085444.
(14) Rosławska, A.; Merino, P.; Große, C.; Leon, C. C.; Gunnarsson, O.; Etzkorn, M.; Kuhnke, K.; Kern, K. *Nano Lett.* **2018**, *18*, 4001−4007.
(15) Yoshioka, K.; Katayama, I.; Arashida, Y.; Ban, A.; Kawada, Y.; Konishi, K.; Takahashi, H.; Takeda, J. *Nano Lett.* **2018**, *18*, 5198−5204.
(16) Yoshioka, K.; Katayama, I.; Minami, Y.; Kitajima, M.; Yoshida, S.; Shigekawa, H.; Takeda, J. *Nat. Photonics* **2016**, *10*, 762−765.
(17) Cocker, T. L.; Peller, D.; Yu, P.; Repp, J.; Huber, R. *Nature* **2016**, *539*, 263−267.
(18) Rashidi, M.; Burgess, J. A. J.; Taucer, M.; Achal, R.; Pitters, J. L.; Loth, S.; Wolkow, R. A. *Nat. Commun.* **2016**, *7*, 13258.
(19) Yoshida, S.; Yokota, M.; Takeuchi, O.; Oigawa, H.; Mera, Y.; Shigekawa, H. *Appl. Phys. Express* **2013**, *6*, 032401.
(20) Li, S.; Chen, S.; Li, J.; Wu, R.; Ho, W. *Phys. Rev. Lett.* **2017**, *119*, 176002.
(21) Zheng, X.; Wang, F.; Yam, C. Y.; Mo, Y.; Chen, G. H. *Phys. Rev. B: Condens. Matter Mater. Phys.* **2007**, *75*, 195127.
(22) Zheng, X.; Chen, G. H.; Mo, Y.; Koo, S. K.; Tian, H.; Yam, C. Y.; Yan, Y. J. *J. Chem. Phys.* **2010**, *133*, 114101−114111.
(23) Terada, Y.; Yoshida, S.; Takeuchi, O.; Shigekawa, H. *Nat. Photonics* **2010**, *4*, 869−874.
(24) Dolocan, A.; Acharya, D. P.; Zahl, P.; Sutter, P.; Camillone, N. *J. Phys. Chem. C* **2011**, *115*, 10033−10043.
(25) Bakulin, A. A.; Silva, C.; Vella, E. *J. Phys. Chem. Lett.* **2016**, *7*, 250−258.
(26) Karki, K. J.; Widom, J. R.; Seibt, J.; Moody, I.; Lonergan, M. C.; Pullerits, T.; Marcus, A. H. *Nat. Commun.* **2014**, *5*, 5869.
(27) Gelin, M. F.; Egorova, D.; Domcke, W. *J. Chem. Phys.* **2009**, *131*, 194103.
(28) Gelin, M. F.; Egorova, D.; Domcke, W. *Acc. Chem. Res.* **2009**, *42*, 1290−1298.
(29) Tretiak, S.; Chernyak, V.; Mukamel, S. *J. Phys. Chem. B* **1998**, *102*, 3310−3315.

DOI: 10.1021/acs.nanolett.9b02389
Nano Lett. 2019, 19, 7006−7012

(30) Jauho, A.-P.; Wingreen, N. S.; Meir, Y. *Phys. Rev. B: Condens. Matter Mater. Phys.* **1994**, *50*, 5528−5544.
(31) Hu, J.; Xu, R.-X.; Yan, Y. J. *J. Chem. Phys.* **2010**, *133*, 101106.
(32) Zhang, Y.; Chen, S. G.; Chen, G. H. *Phys. Rev. B: Condens. Matter Mater. Phys.* **2013**, *87*, 085110.

DOI: 10.1021/acs.nanolett.9b02389
Nano Lett. 2019, 19, 7006−7012

Supporting information

STM Imaging of electron migration in real space and time: a simulation study

YanHo Kwok,[1,2] *GuanHua Chen,*[1, a)] *and Shaul Mukamel*[3, b)]

[1] Department of Chemistry, the University of Hong Kong, Pofkulam Road, Hong Kong,

[2] QuantumFabless Limited, Sha Tin, Hong Kong,

[3] Department of Chemistry and Physics and Astronomy, University of California, Irvine, California 92617, United States

Effect of pulse-width and frequency

The choices of pulse-width and frequency are important to obtain a good agreement between the time-dependent populations and the integrated current signals. Figure S1 shows the excited populations of site 1-6 after the illumination of a single laser pulse with central frequency ω and full-width at half-maximum (FWHM) = 20 fs. The peak positions correspond to the HOMO-LUMO gaps of the corresponding sites while the peak widths are determined by the pulse-width and the line width due to the electrodes.

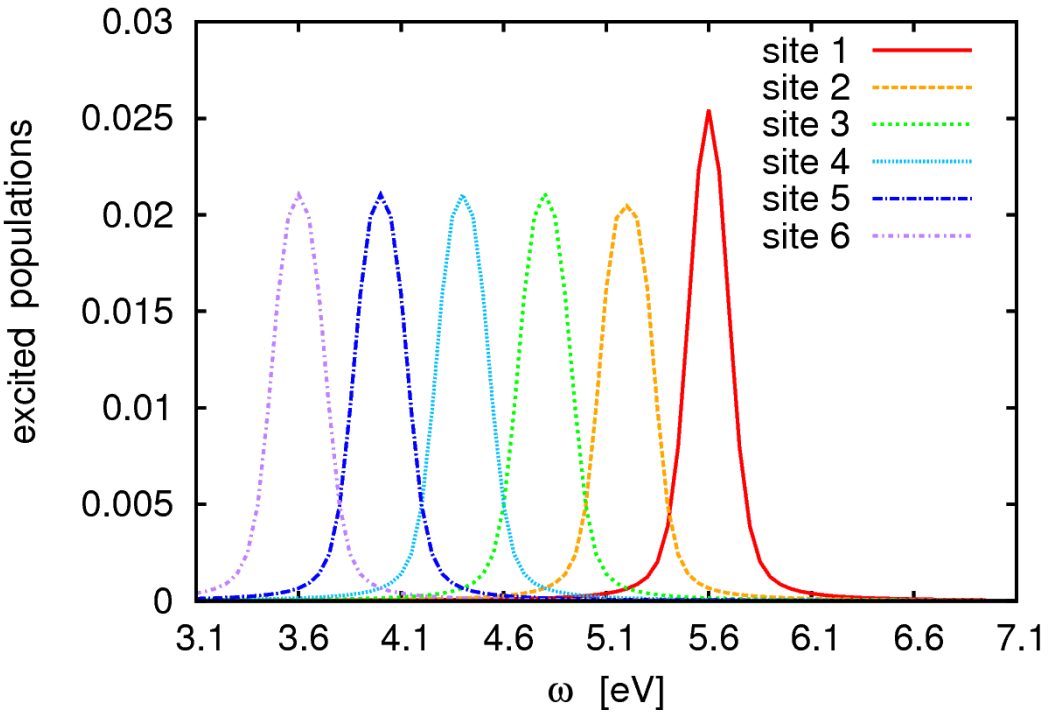

Figure S1. Excited populations on site 1-6 after a single laser pulse with frequency ω and FWHM = 20fs.

The time-resolution of a pump-probe experiment is limited by the width of the pulses. Therefore the pulse-width has to be comparable to or shorter than the timescale of phenomenon of interest. On the other hand, a short pulse also means a wide bandwidth in the energy domain and this will cause unwanted excitation of the other sites even though the frequency of the pulse is not in resonant with them. This unwanted excitation will finally lead to unwanted current signal. Here, we compare simulation results with FWHM being set to 12fs and 20fs (both pump and probe pulse have the same FWHM), which are shown in Figure S2. Other parameters remain the same as given in the main text. We can see that even for FWHM = 12fs, the integrated current curves still follow the time-dependent populations. But we will see that the larger bandwidth does cause more unwanted current due to excitations of nearby sites.

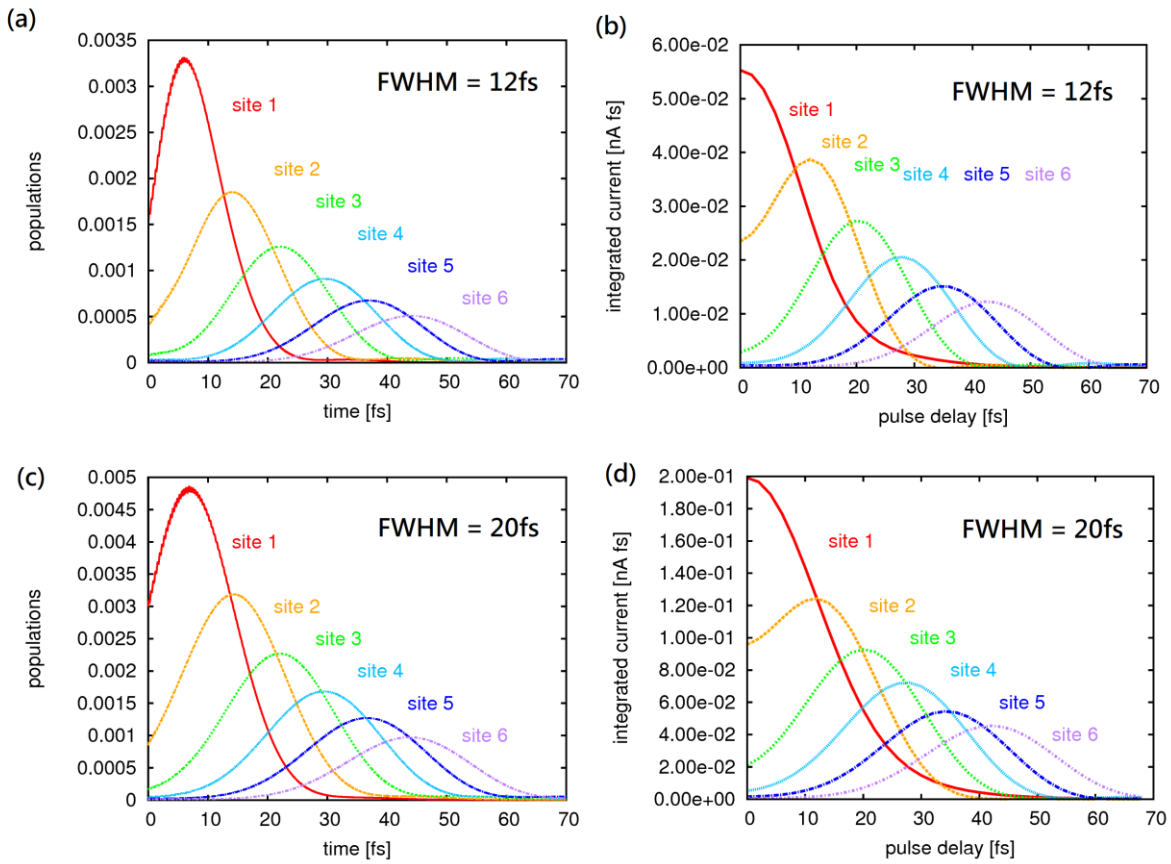

Figure S2. (a) Populations versus real time for sites 1-6 with FWHM = 12fs. (b) Integrated current versus pump-probe pulse delay for tip located at site 1-6 with FWHM = 12fs. For the tip located at site 1, the magnitude is reduced by 3 times. (c) Populations versus real time for sites 1-6 with FWHM = 20fs. (d) Integrated current versus pump-probe pulse delay for tip located at site 1-6 with FWHM = 20fs. For the tip located at site 1, the magnitude is reduced by 3 times.

The integrated current resulting from unwanted excitation can be estimated by modifying the dipole matrix $\boldsymbol{\mu}$ such that the pump can only excite site 1 while the probe can only excite the site under tip. This would give the current free from unwanted excitation, which is shown as point curves in Figure S3. The original integrated currents are plotted as line curves for reference. The difference between the line curves and point curves corresponds to the unwanted current. The unwanted current is significant and contributes to the total current for a large portion when the pulse delay is short. This is due to the large population of site 1 just after the pump pulse arrives, therefore unwanted excitation of site 1 by the probe will cause a significant additional current. Also, the additional current with FWHM = 12fs is more significant than that with FWHM = 20fs, which is expected due to the larger energy bandwidth of the pulses.

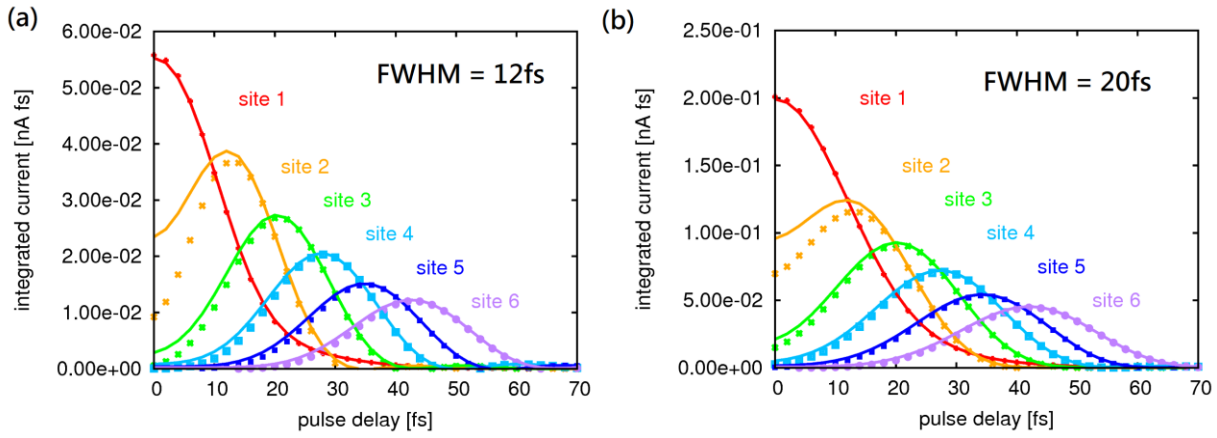

Figure S3. Integrated current versus pulse delay for tip at site 1-6 respectively with (a) FWHM = 12fs and (b) FWHM = 20fs. Solid line curves are integrated current with unwanted excitation. Point curves are integrated current free from unwanted excitation (obtained by modifying dipole matrix so that pump pulse only excites site 1 and probe pulse only excites the tip-probing site). For the tip located at site 1, the magnitude is reduced by 3 times.

Effect of coupling with substrate

The coupling between the system and the substrate leads to dissipative effect which drives the excited system back to equilibrium gradually. Such effect is quantified by the linewidth matrix. The larger the linewidth, the faster the dissipation occurs and the excited populations decay faster. In the manuscript, the linewidth matrix due to coupling with the substrate is diagonal with value equal to 0.02eV for the LUMO. This value is comparable to the choice of hopping among sites, which is 0.05eV, and the excited electrons in the LUMO dissipate in the timescale of around tens of femtoseconds. In reality, the molecule may be placed on a thin decoupling layer to avoid strong coupling with the substrate. To simulate that situation, we reduce the linewidth of the LUMO due to the substrate by 10 times, from 0.02eV to 0.002eV, which would lead to a much slower decay of the populations. All the other parameters are kept the same. Fig. S4(a) shows the time-dependent populations in this case. We can see that the populations decay much slower. Figure S4(b) shows the integrated current versus pulse delay. We can see that the curves still follow with the time-dependent populations.

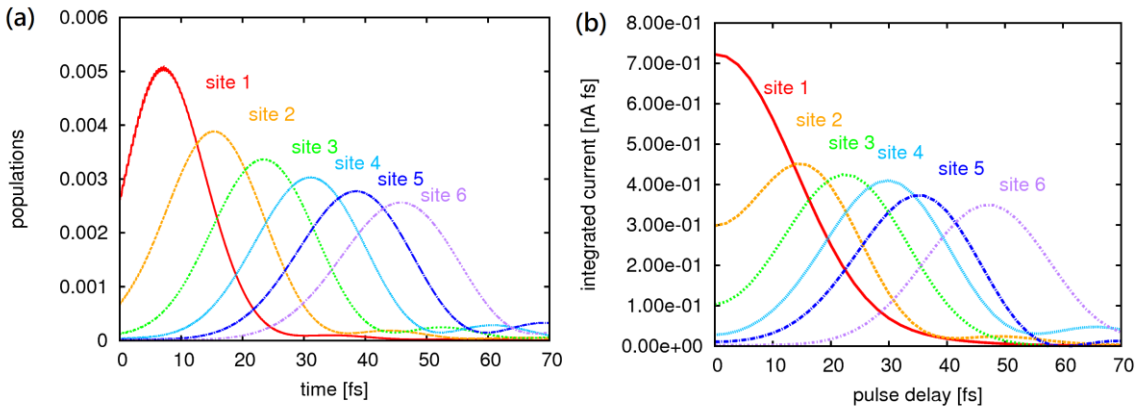

Figure S4. Simulation results with reduced linewidth. (a) LUMO populations of sites 1-6 induced by the pump. (b) Integrated current versus pulse delay for tip at site 1-6 respectively. For the tip located at site 1, the magnitude is reduced by 3 times.

Charge injection and the effect of asymmetric pulses

As mentioned in the main content, the laser pulses can affect the system in two ways. First, the laser pulses can excite electrons from HOMO to LUMO when the frequency is resonant with the HOMO-LUMO gap. Second, when the polarization of the electric field is parallel to the tip-substrate direction, a significant transient bias voltage can be induced due to field enhancement. The induced transient voltage can cause the injection of electrons from the electrodes.

Here, we attempt to estimate the effect of electron injection when the field is polarized along tip-substrate direction. Let us recall that the incident electric field is of the form

$$E(t) = \mathcal{E}_1(t)\cos(\omega_1 t) + \mathcal{E}_2(t)\cos(\omega_2 t).$$

We assume that after field-enhancement, a transient voltage of the same form, with peak voltage equals to 2.0V, is induced across the junction. This value is large but possible in experiments

considering the fact that the field enhancement factor can be over thousands[1,2]. Since the LUMO of the sites are 1.5 eV above the Fermi level while HOMO are 0.7 – 2.5 eV below, for temperature at 300K, this induced voltage in principle allows electron injection into or out of the system.

The actual distribution of the enhanced field depends on the actual system of interest. Here, we still treat the enhanced field by the dipole approximation. And we assume the tip-substrate distance is 10Å so that the enhanced field would be 0.2 V/Å. The transition dipole matrix elements for all sites are assumed to be 0.2 eÅ. This value is smaller than that when the field is perpendicular to the tip-substrate direction because we assume the molecule under study is lying approximately flat on the substrate. Other parameters, such as the line width, pulse width and the DC voltage, remain the same as given in the main text. The transient bias voltage $V_\alpha(t)$ is taken into account in our equation of motion for the dissipative matrices.

$$\boldsymbol{\varphi}_{\alpha,p}(t) = -iR_p \int_{-\infty}^{t} d\tau \mathbf{G}_D^r(t,\tau)\boldsymbol{\Gamma}_\alpha \exp\left(-i\int_t^\tau dt' \, \varepsilon_{\alpha,p} + V_\alpha(t')\right).$$

$$i\frac{d}{dt}\boldsymbol{\varphi}_{\alpha,p}(t) = -iR_p\boldsymbol{\Gamma}_\alpha + \left[h_D - \frac{i}{2}\boldsymbol{\Gamma} - \varepsilon_{\alpha,p} - V_\alpha(t)\right]\boldsymbol{\varphi}_{\alpha,p}(t),$$

Figure S5 shows the results with effect of transient bias taken into account. First of all, figure S5(a) shows the time-dependent populations for the LUMO of sites 1-6 due to the pump. The arrival time of the center of the pump pulse is set to zero. The transient voltage causes electron injection from the electrodes occurs when the pump pulse arrives and contributes to additional populations on the LUMO of the sites. Such additional populations are plotted versus time in figure S5(b). The populations gradually increase during the pump but are highly oscillatory due to the highly oscillating transient voltage which drives the current in and out the system. This approximated cancellation of positive and negative transient currents make the net electrons

injected small compared to the populations due to resonant excitation. After the pump, the injected populations gradually leave through the electrodes. Figure S5(c) shows the summation of such additional populations again for sites 1-6 but with different phase-shifted pump pulse.

$$E(t) = \mathcal{E}_1(t)\cos(\omega_1 t + \phi)$$

Such phase shift can introduce significant asymmetry for single-cycle THz pulses[2,3]. But since we are using multi-cycles pulse that last for tens of periods, shifting the phase only has little effect on the symmetry. Thus the results are similar. Figure S5(d) shows the integrated current versus pulse delay for tip at site 1-6. Electron injection due to transient bias also affects the integrated current signal, contributing to additional integrated current for short pulse delay. Nevertheless, the integrated current signals still follow the populations.

Finally, it is remarked that the electric field (0.2V/Å) we are considering here is indeed large and it may cause tunneling field emission. We simulate this situation in order to demonstrate that the electron injection would not cause a problem even at such induced transient voltage. In reality, we can of course reduce the incident field strength according to the field enhancement factor to avoid field emission.

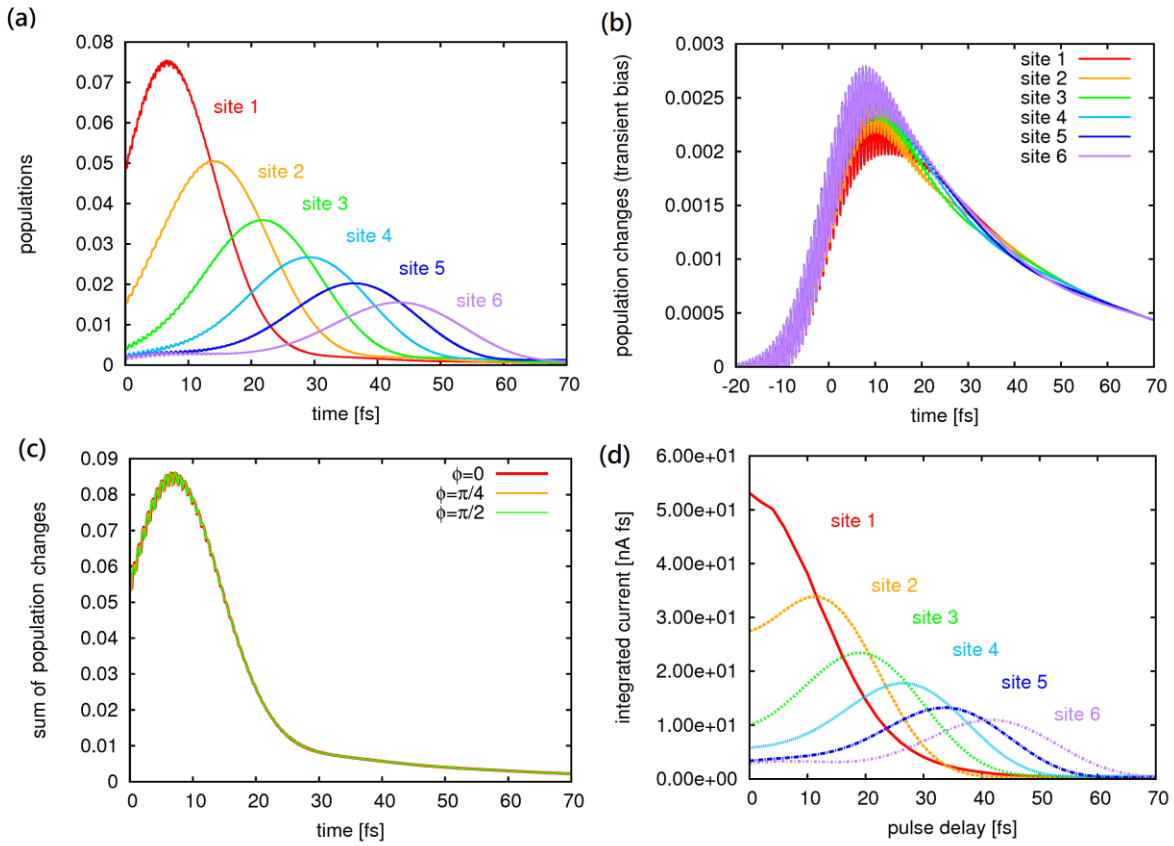

Figure S5. Simulation results with transient bias effect. (a) LUMO occupations of sites 1-6 induced by the pump. (b) LUMO occupation changes of sites 1-6 due to the induced transient voltage (c) summation of the occupation changes for sites 1-6 due to the induced transient voltage for different phase for the pump pulse. (d) Integrated current versus pulse delay for tip at site 1-6 respectively. For the tip located at site 1, the magnitude is reduced by 3 times.

System with varying LUMO energies

In the model presented in the main content, we assume the same LUMO energies (1.5eV above the Fermi level) for all sites for simplicity. Here, we consider a system with gradually decreasing LUMO energies. The LUMO energies of the 10 sites are 1.5, 1.47, 1.44, 1.41, 1.38, 1.35, 1.32, 1.29, 1.26 and 1.23 eV respectively. The difference between LUMO energies of neighboring

sites is comparable to the hopping (0.05 eV), so the charge migration still occurs smoothly. Again, the central frequency of the pump is 5.6 eV and the central frequency of the probe is chosen to be resonant with the HOMO-LUMO gap of the site under the STM tip. All the other parameters are kept the same. Figure S6(a) shows the time-dependent populations in this case and figure S6(b) shows the integrated current versus pulse delay. Compared to the original model, the time-dependent populations in this case show additional peaks at later time due to the varying LUMO energies. Still, the integrated current curves follow the time-dependent populations.

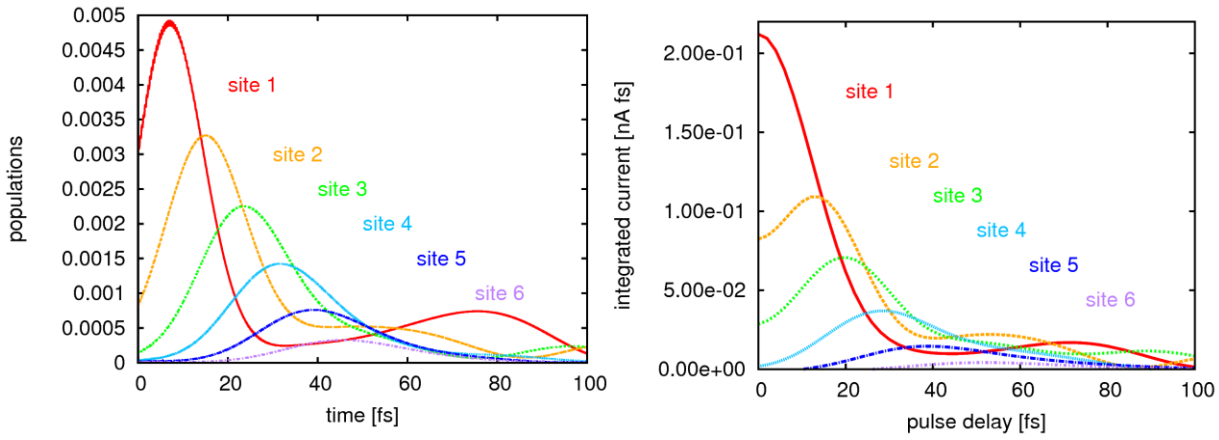

Figure S6. Simulation results with varying LUMO energies. (a) LUMO populations of sites 1-6 induced by the pump. (b) Integrated current versus pulse delay for tip at site 1-6 respectively. The magnitude is reduced by 4 times for tip at site 1 and 1.5 times for tip at site 2.

References

(1) Cocker, T.; Jelic, V.; Gupta, M. *Nat Photonics* **2013**, *7*, 620–625.

(2) Yoshioka, K.; Katayama, I.; Minami, Y.; Kitajima, M.; Yoshida, S.; Shigekawa, H.; Takeda, J. *Nat. Photonics* **2016**, *10*, 762–765.
(3) Cocker, T. L.; Peller, D.; Yu, P.; Repp, J.; Huber, R. *Nature* **2016**, *539*, 263–267.